Advanced Composites and Hybrid Materials (2023) 6:60
https://doi.org/10.1007/s42114-023-00637-0

RESEARCH

Proton-conductive channels engineering of perfluorosulfonic acid membrane via in situ acid–base pair of metal organic framework for fuel cells

Wenxing Zhang[1,2] · Shengqiu Zhao[1,2] · Rui Wang[1,2] · Aojie Zhang[1,2] · Yi Huang[3] · Haolin Tang[1,2]

Received: 15 December 2022 / Revised: 7 February 2023 / Accepted: 28 February 2023 / Published online: 14 March 2023

Abstract

The development of rapid and dependable proton transport channels is crucial for proton exchange membrane fuel cells (PEMFCs) operating in low humidity conditions. Herein, a metal–organic framework (NH-Zr framework) consisting of 1H-pyrazole-3, 5-dicarboxylic acid (PZDC), and zirconium chloride octahydrate ($ZrOCl_2 \cdot 8H_2O$) rich in basic sites was in situ constructed in a perfluorosulfonic acid (PFSA) solution, and hybrid proton exchange membranes were prepared (PFSA-NH-Zr). The introduced NH-Zr framework successfully induced proton conducting groups ($-SO_3H$) reorganization along the NH-Zr framework, resulting in the formation of fast ion transport channels. Meanwhile, under low humidity, the acid–base pairs between N–H (NH-Zr framework) and $-SO_3H$ (PFSA) promoted the protonation/deprotonation and the subsequent proton leap via the Grotthuss mechanism. Especially, the hybrid membrane PFSA-NH-Zr-1 with suitable NH-Zr content had a promising proton conductivity of 0.031 S/cm at 80 °C, 40% relative humidity (RH), and 0.292 S/cm at 80 °C, 100% RH, which were approximately 33% and 40% higher than the pristine PFSA membrane (0.023 S/cm and 0.209 S/cm), respectively. In addition, the maximum power density of the hybrid proton exchange membrane was 0.726 W/cm^2, which was nearly 20% higher than the pristine PFSA membrane (0.604 W/cm^2) under 80 °C, 40% RH. Thus, PFSA-NH-Zr may be promising membrane materials for potential applications in fuel cells. This work established a referable strategy for developing high-performance proton exchange membranes under low RH conditions.

Keywords Proton exchange membrane · Proton-conducting channels · Acid–base pairs · Grotthuss mechanisms · Proton conductivity

1 Introduction

Due to the characteristics of excellent energy conversion efficiency, low environmental pollution, and fast start-up and shut-down, proton exchange membrane fuel cell has been recognized as critical green equipment for applications involving mobile equipment, residential buildings, and portable power generation [1–13]. Being the pivotal component of PEMFC, proton exchange membranes serve as an electrolyte for proton transport and as a separator for reactant gases. High proton conductivity, low fuel permeability, and good physicochemical stability are the requirements for proton exchange membranes to achieve high efficiency and high stability in fuel cell operation [14–20].

Currently, perfluorosulfonic acid membranes, for instance, Nafion, are popularly used PEMs with high proton conductivity within a given temperature and humidity range [21–24]. Sulfonic groups could assemble to form ion

Wenxing Zhang and Shengqiu Zhao contributed equally to this work.

✉ Haolin Tang
thln@whut.edu.cn

[1] State Key Laboratory of Advanced Technology for Materials Synthesis and Processing, Wuhan University of Technology, Wuhan 430070, China

[2] Foshan Xianhu Laboratory of the Advanced Energy Science and Technology Guangdong Laboratory, Xianhu Hydrogen Valley, Foshan 528200, China

[3] State Key Laboratory of Automotive Safety and Energy, School of Vehicle and Mobility, Tsinghua University, Beijing 100084, China

clusters and build well-interacted hydrophilic channels for proton-conduction under hydration conditions, which readily achieve adequate proton conductivity (~0.1 S/cm) [25]. However, at low relative humidity (RH) environment, the ionic clusters are not connected, thereby it is hard for protons to diffuse through the membrane due to the conduction mechanism of short-range proton hopping, resulting in low proton conductivity and thus reducing the electrochemical performance of PEM [26–31].

To promote the performance of the membrane at low relative humidity, several methods have been investigated, such as developing non-fluorinated polymers [32], replacing acid groups such as sulfonic or phosphoric acids with heterocyclic compounds for example imidazole or triazole [33], and incorporating hygroscopic inorganic nanomaterials to prepare inorganic–organic composite membranes [34]. Studies have shown that inorganic–organic composite membranes are very promising due to their ability to maintain high water retention and proton conductivity at relatively low relative humidity [35–40]. In addition, they restrain excessive swelling of the PEM while ensuring the mechanical properties of the polymer chains under harsh conditions and preventing degradation. Our groups proved that the self-assembled inorganic nanoparticles enhanced the water retention performance of the hybrid membrane at high temperature and low relative humidity compared to the conventional Nafion/silica hybrid and pristine Nafion 212 membranes by incorporating hygroscopic metal oxide particles SiO_2 into the hydrophilic domains of the electrolyte, and enhanced the Nafion/silica nanocomposite membrane stability [41, 42]. Furthermore, Hasmukh blended a superacid sulfonated Zr-MOF (SZM) into Nafion and the significant amount of water in SZM networks due to the Brønsted acidic sites promoted proton conduction at low humidity [43]. Although the low-humidity proton conductivity of the membrane could be improved by introducing the inorganic filler with excellent water retention ability, the proton conductive channel (PCC) originally present in the Nafion membrane would be disrupted during the traditional recasting process and hence damage the proton conductivity of the Nafion membranes [44, 45].

In recent years, the strategy of "acid–base pairs" construction has been regarded as an effective approach to improve the ion conduction channel and enhance ion conductivity. Wieczorek and Chen tested the PAN/$LiClO_4$ with the Al_2O_3 system to prove that the Lewis acid–base pair contributes to the separation of the $LiClO_4$ ion pair, leading to an increase of free ions, while the intermittent coordination could enhance the ion transference number and ionic conductivity by providing a continuous channel for the charge carrier transport [46, 47]. Hence, the method of preparing acid–base pairs was considered a potential means to improve the proton conductivity of hybrid membranes. The existence of acid–base pairs promotes protonation/deprotonation and generates a significant amount of proton defects, thereby paving the transport pathway for proton hopping at low energy barriers [48]. Moreover, the intense electrostatic interactions between acid–base pairs could inhibit the movement of neighboring polymer chains, thus enhancing the water stability and the mechanical properties of the membrane. However, the synthesis of acid–base hybrid membranes by simply filling inorganic materials will lead to the reunion of inorganic particles and the discontinuity in the proton transport pathway, which will hinder the further improvement of proton transmission efficiency and proton conductivity [49].

Metal–organic frameworks (MOFs) are exceptional porous materials that have been proven to be candidates for proton-conducting applications due to their designability and chemical stability [50–57]. Zhuang fabricated a proton exchange membrane possessing acid–base pairs by adding DHZIF-8 to the Nafion matrix, increasing the proton conductivity to 0.255 S/cm and 3.66 mS/cm (0.104 S/cm and 1.14 mS/cm for Nafion control membrane, respectively) at 80 °C, 95% RH, and 120 °C, anhydrous environment, respectively [49]. Wang reported a Zn-MOF/Nafion hybrid membrane in which the proton conduction groups were induced to reorganize along the Zn-MOF to form long-range ordered proton conduction pathways, which facilitated the improvement of proton conductivity of the membrane and the overall performance of the fuel cell [50]. Therefore, constructing a framework structure containing basic sites in the perfluorosulfonic acid matrix and forming acid–base pairs with sulfonic acid groups is expected to build fast proton transport channels in the form of acid–base pairs to facilitate proton conduction.

In this study, the NH-Zr framework structure rich in basic sites were constructed in situ by adding PZDC and $ZrOCl_2{\cdot}8H_2O$ to the PFSA solution, and the mixture was cast to obtain the PFSA-NH-Zr hybrid membrane (Fig. 1). The introduced NH-Zr framework effectively induced the reorganization of the proton conducting group (-SO_3H) along the NH-Zr framework, thus constructing a fast ion transport channel. Meanwhile, the acid–base pairs between N–H (NH-Zr framework) and -SO_3H (PFSA) promoted the protonation/deprotonation and the subsequent proton leap via Grotthuss mechanisms under low humidity. These significantly accelerated the proton conduction of the hybrid membranes. Specifically, the hybrid membrane loaded with 0.075 mg/cm^2 PFSA-NH-Zr showed a proton conductivity of up to 0.031 S/cm at 80 °C, 40% RH, and 0.292 S/cm under 80 °C and 100% RH. The effects of NH-Zr loading on membrane morphology, water uptake, and thermal stability were also investigated. This study guided the development of high-performance proton exchange membranes under low humidity conditions.

2 Materials and methods

2.1 Materials andpreparation

1H-pyrazole-3, 5-dicarboxylic acid (PZDC), Zirconium chloride octahydrate ($ZrOCl_2 \cdot 8H_2O$), N, N'-dimethylformamide (DMF), and formic acid were provided from Aladdin Industrial Corporation (Shanghai, China). A perfluorosulfonic acid resin having two carbon-ether side chains (D79, EW790) was provided by Solvay Company (Bollate, Italy). Sulfuric acid (H_2SO_4, 98 wt%) was provided by Tianjin Damao Chemical Reagent Co., Ltd.

2.2 Preparation of mixed resin solution

After evaporation of the D79 solution, the resulting resin was dissolved in DMF (15 g) and stirred continuously for 6 h to form a homogeneous and clear solution. Then PZDC (0.5 mmol, 87 mg) was joined to the clear solution and stirred continuously for 30 min. $ZrOCl_2 \cdot 8H_2O$ (0.435 mmol, 140 mg) and 10 mL formic acid was added and stirred for 1 h, then transfer the mixture to an internal autoclave (50 mL) of Teflon and placed at 130 °C for 3 days. Finally, the mixed resin solution of PFSA-NH-Zr was obtained after ultrasonic stirring for 4 h and Magnetic stirring for 12 h.

2.3 Preparation of hybrid membranes

The PFSA-NH-Zr hybrid membrane was obtained by the flow-casting method. Specifically, the PFSA-NH-Zr hybrid resin solution was cast on the flat glass, dried at 50 °C for 12 h, and then placed at 140 °C for 2 h for annealing treatment to improve the crystallinity of the membrane. To improve the acidity as well as the ionic conductivity, all the prepared membranes were soaked in 2.5 wt% H_2SO_4 (80 °C) solution for 30 min and then transferred to 1 L deionized water (80 °C) for 30 min, repeating three times, followed by final drying at 60 °C to obtain PFSA-NH-Zr hybrid membrane. These hybrid membranes were named PFSA-NH-Zr-X, where X is the weight ratio percentage of inorganic filler. All membranes had a thickness within the range of 26 ± 1 μm.

2.4 Material characterization

Morphological characterization High resolution-scanning electron microscope (FE-SEM, Zeiss Ultra Plus) fitted with an X-ray energy spectrometer (X-Max 50) was used to observe the morphologies of samples. Before observation,

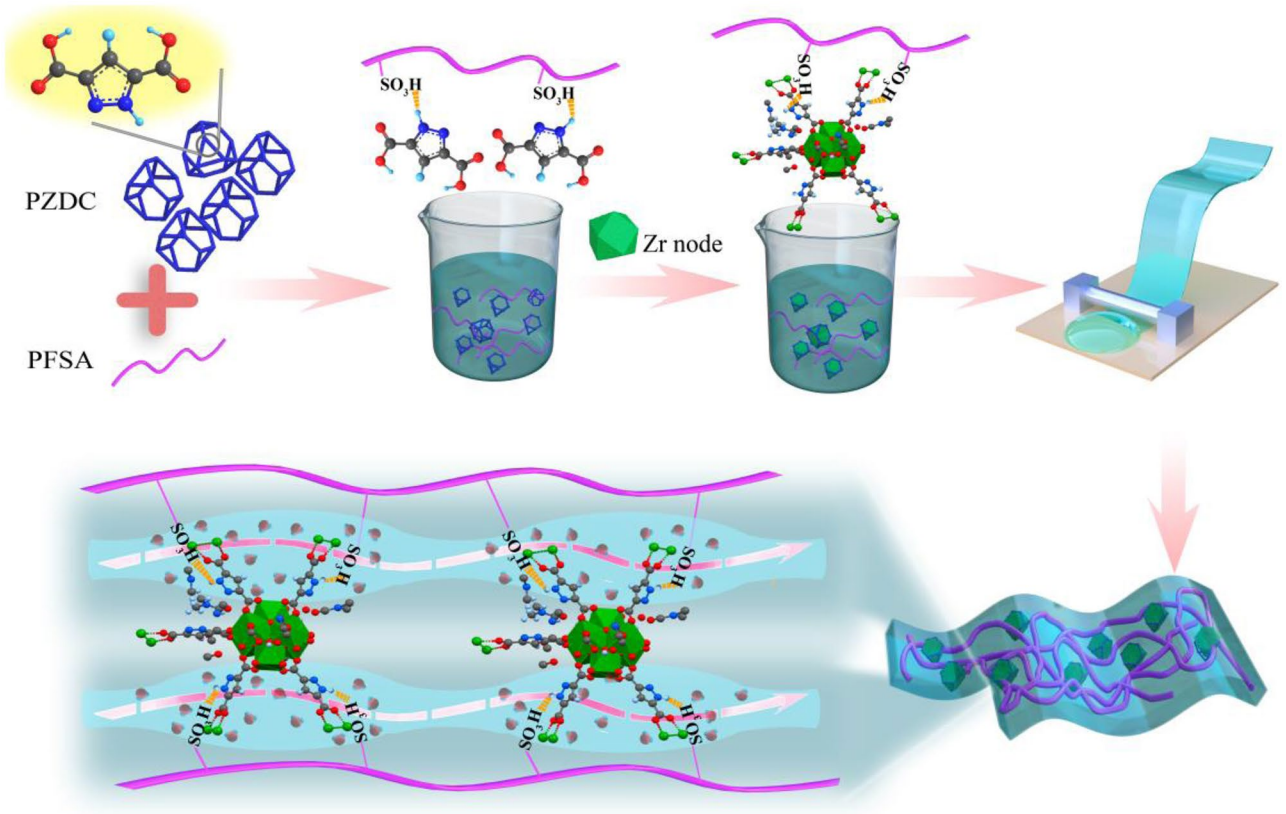

Fig. 1 Schematic diagram of the procedure for fabricating a hybrid membrane with NH-Zr framework

the specimens were sputtered with platinum. SEM energy-dispersive spectroscopy (EDS) was utilized to analyze the chemical composition of PFSA-NH-Zr-X. An atomic force microscope (AFM, Bruker, Fastscan) in mechanical properties mode was utilized to further observe the morphology of the specimens [58].

Structural and elemental characterizations Powder X-ray diffraction (PXRD, Bruker D8 diffractometer) was used to study the crystallinity of the sample. Thermogravimetric analysis (TGA, TA instruments) and differential scanning calorimetry (DSC, TA Instruments) under an N_2 atmosphere were used to study the thermal properties of the samples [59, 60]. TGA curves and DSC analysis were performed in temperatures range of 30–800 °C and − 50 to 200 °C, respectively, both at a heating speed of 10 °C/min. The DSC curve was used to confirm the glass transition temperature (Tg) of the specimen. X-ray photoelectron spectroscopy (XPS, AxisNova) was utilized to probe the sample chemical structure.

Water uptake, swelling Water uptake and dimensional swelling of the membranes were derived by measuring the difference in weight and area. Dried membranes of a certain area (4 × 4 cm) were weighed, and then the weight and area of the membranes were measured again after immersing them in distilled water at 80 °C for 12 h. The WU and SR values of all samples were calculated as follows:

$$\mathrm{WU} = \frac{(M_{\mathrm{wet}} - M_{\mathrm{dry}})}{M_{\mathrm{dry}}} \times 100\% \tag{1}$$

$$\mathrm{SR} = \frac{(S_{\mathrm{wet}} - S_{\mathrm{dry}})}{S_{\mathrm{dry}}} \times 100\% \tag{2}$$

where M_{wet} and M_{dry} are the weights of the wet and dry samples, while S_{wet} and S_{dry} are the areas of the wet and dry samples, respectively. The final results were calculated via the average of at least three parallel measurements with accuracy within ± 4.0%. A contact angle goniometer (DSA10, Kruss GmbH) was used to measure the contact angle of water at room temperature to characterize the surface hydrophilicity of the membrane specimens.

Proton conductivity, activation energy An electrochemical workstation (Metrohm Autolab 302 N) in the range of 0.1–1 MHz by AC impedance technique was utilized to confirm the proton conductivity (σ) of the specimens. The experiments were performed under variable conditions of 100% humidity and relative temperature (30, 40, 50, 60, 70, 80, and 90 °C, respectively) in a temperature-controlled humidity climatic chamber, and the specimens were placed in a water-flooded environment for 4 h, followed by conductivity testing at an electrochemical workstation. The membrane proton conductivity is calculated as follows:

$$\sigma(\mathrm{S/cm}) = \frac{L}{R \times S} \tag{3}$$

where L is the distance between the two electrodes, while R and S represent the resistance and cross-sectional area of the membrane, respectively.

The activation energy (Ea) values for each membrane were obtained by least-squares fitting based on Arrhenius plots as follows:

$$\sigma(\mathrm{S/cm}) = A\exp\left(\frac{-E_a}{R \times T}\right) \tag{4}$$

where σ and A are the proton conductivity and pre-exponential factor, while R and T represent the molar gas constant and temperature.

Single-cell performance Membrane electrode assemblies (MEAs) were fabricated into the sandwich structure. The coated catalyst layers (0.4 mg Pt/cm^2 on the cathode and 0.1 mg Pt/cm^2 on the anode) were heat pressed on both sides of the membrane, provided by Wuhan Polytechnic Hydrogen Technology Co. Before testing the polarization curves of the PEMFC, the anode, and cathode of the single cell were fed with hydrogen and air, respectively, to activate the fuel cell to reach steady state, with a stoichiometric ratio of 1.5 and 2.0 hydrogen to air, a minimum flow rate of 1000 sccm/min and 2000 sccm/min respectively, and partial pressure of 150 kPa for the inlet gas. In the hydrogen crossover test, both the hydrogen delivered to the anode and the nitrogen delivered to the cathode of the cell were dosed at 200 sccm, and swept from 0 to 0.7 V at 30 °C using linear sweep voltammetry (LSV) with a sweep speed of 2 mV/s and no back pressure. Notice that the current density at a voltage of 0.3 V was regarded as the hydrogen crossover value of the membrane. The EIS measurement was performed with a current density of 800 mA/cm^2 and a frequency range of 0.5–20 kHz for the measurement of proton conduction resistance.

3 Results and discussion

3.1 Characterization of the membranes

The micromorphology of the hybrid membranes (PFSA-NH-Zr-1 and PFSA-NH-Zr-10) and the distribution of the doped NH-Zr framework in the membranes were observed by SEM. As shown from the surface SEM image in Fig. 2, the synthesized NH-Zr framework showed a truncated cubic shape in the nanometer size range of about 100–200 nm, which was

uniformly dispersed within the hybrid membranes. Meanwhile, these hybrid membranes had a uniform structure with no fractures or pin holes as well as no gaps on the surface, which indicated that the preparation of the membranes was successful. The surface SEM image showed a pristine PFSA membrane and PFSA-NH-Zr-1 membrane was compact and smoothed, without indication of phase-separation (Fig. 2a, b), suggesting that the perfluorosulfonic acid matrix had good compatibility with the NH-Zr framework in the hybrid membranes, which might be attributed to the strong intermolecular interactions to form a robust covalent interface. The homogeneous dispersion of the filler and the good compatibility between the polymers were thought to assure more continuous pathways for proton transfer. The cross-sectional SEM images of PFSA-NH-Zr-1 presented a lamellar comparatively compact morphological structure similar to that of PFSA (Fig. 2d, e), and there was no indication of phase separation. Meanwhile, the elemental mapping distribution on the surface of PFSA-NH-Zr-1 was shown in Fig. 2g, h, where the elements Zr and N were distributed evenly on the surface of the hybrid membrane. As the filler loading increased to 5 wt%, we could observe that the particles on the surface of the hybrid film started to appear as aggregates (Fig. S1). As can be seen from Fig. 2c, the cross-section of the PFSA-NH-Zr-10 hybrid membrane became rough with many folds and cracks (Fig. 2f), indicating that the NH-Zr framework became less compatible in the perfluorinated sulfonate matrix with significant aggregation. Such phenomena could also be proved from the corresponding elemental mapping images of Zr, N (Fig. 2i, j).

The AFM analysis was applied to investigate the surface of membranes, and corresponding topographies were shown in Fig. 3. The AFM height distribution (Fig. 3a–c), corresponding line profiles (Fig. 3d–f), and 3D distribution diagram (Fig. 3g–i) showed that the average surface roughness of PFSA-NH-Zr-1 hybrid membrane was only slightly increased compared with the pristine PFSA membrane. The results demonstrated that there was good interfacial compatibility between the NH-Zr framework and perfluorosulfonic acid matrix, which was beneficial to the formation of continuous proton transport pathways between the NH-Zr framework particles and the perfluorinated sulfonate matrix under the action of acid–base proton pairs and promoted the water absorption as well as proton conduction of the membrane. However, the surface roughness of the PFSA-NH-Zr-10 hybrid membrane (Fig. 3f) increased significantly compared to the PFSA-NH-Zr-1 membrane, and the PFSA-NH-Zr-10 hybrid membrane appeared with a large number of aggregations in the three-dimensional distribution diagram (Fig. 3i), which was unfavorable for the formation of a fast proton conduction channel, thus affecting the improvement of proton conductivity.

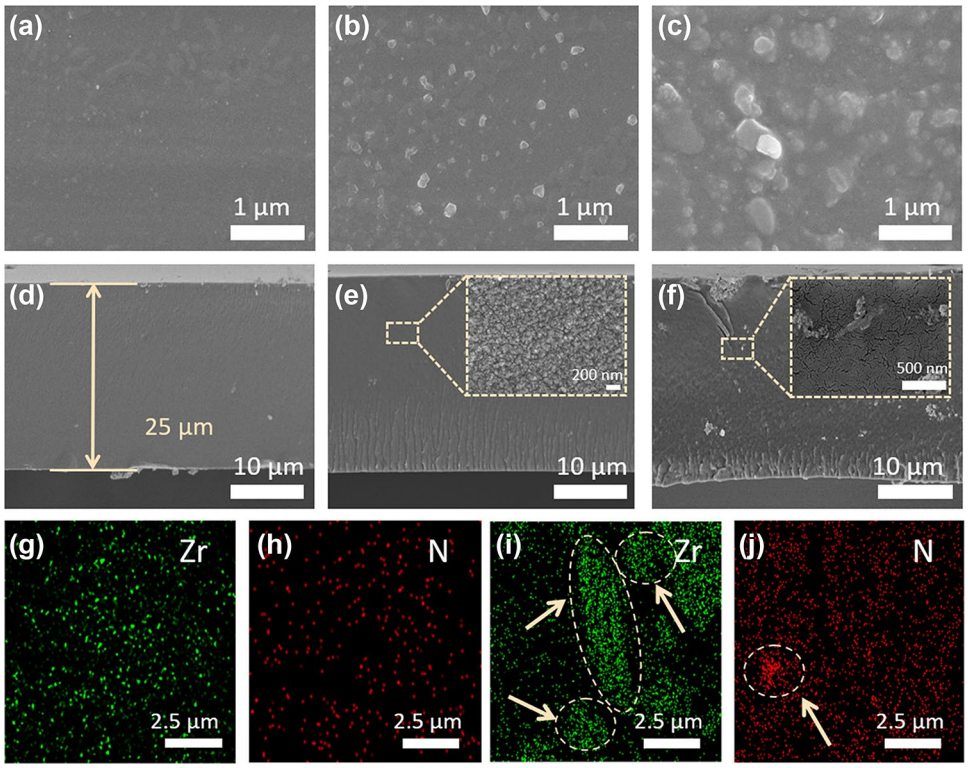

Fig. 2 **a–c** The surface-view SEM images and **d–f** cross-section SEM images of PFSA, PFSA-NH-Zr-1, and PFSA-NH-Zr-10. **g–j** The corresponding elemental mapping images of Zr, N of PFSA-NH-Zr-1 and PFSA-NH-Zr-10. The illustration is a high-resolution image of the chosen area

3.2 Physicochemical properties of the membranes

As could be seen, the positions of the evident diffraction peaks of PFSA-NH-Zr-1 were unchanged except for some changes in lattice strength as compared to the XRD patterns of simulated-MOF-802 (Fig. 4a). This demonstrated that the synthesized NH-Zr framework had a metal frame mechanism, providing a framework basis for the construction of fast proton transport channels. At the same time, it could be found that the PFSA-NHH-Zr-1 characteristic peaks did not change significantly as compared to the pristine PFSA membrane spectra (Fig. 4a), indicating that the NH-Zr framework had good compatibility with perfluorosulfonic acid matrix and had not destroyed the microstructure of perfluorosulfonic acid, thus preserving the original proton transport channel.

The thermal stability of all membranes was defined via TGA analysis, and its results were shown in Figs. 4b and S2. All the hybrid membranes showed similar pyrolysis processes and had three stages of weight loss. The first weight loss below 200 °C was associated with the removal of absorbed water and the second weight loss (290–400 °C) was considered to be the critical mass of SO_3H. The third weight loss (about 450 °C) was associated with the decomposition of the NH-Zr framework. These results showed that all the hybrid membranes had excellent thermal stability. The lower weight loss for the hybrid membrane as compared to the pristine PFSA membrane indicated that the incorporation of the NH-Zr framework inhibited the degradation of the polymer framework as well as improved the thermal stability of the hybrid membrane to some extent.

To evaluate the impact of the NH-Zr framework on the membrane structure, heat flow curves and glass transition temperatures (Tg) were calculated for various membranes (Fig. 4c). The pristine PFSA membrane and PFSA-NH-Zr-1 hybrid membrane had obvious exothermic behavior at the

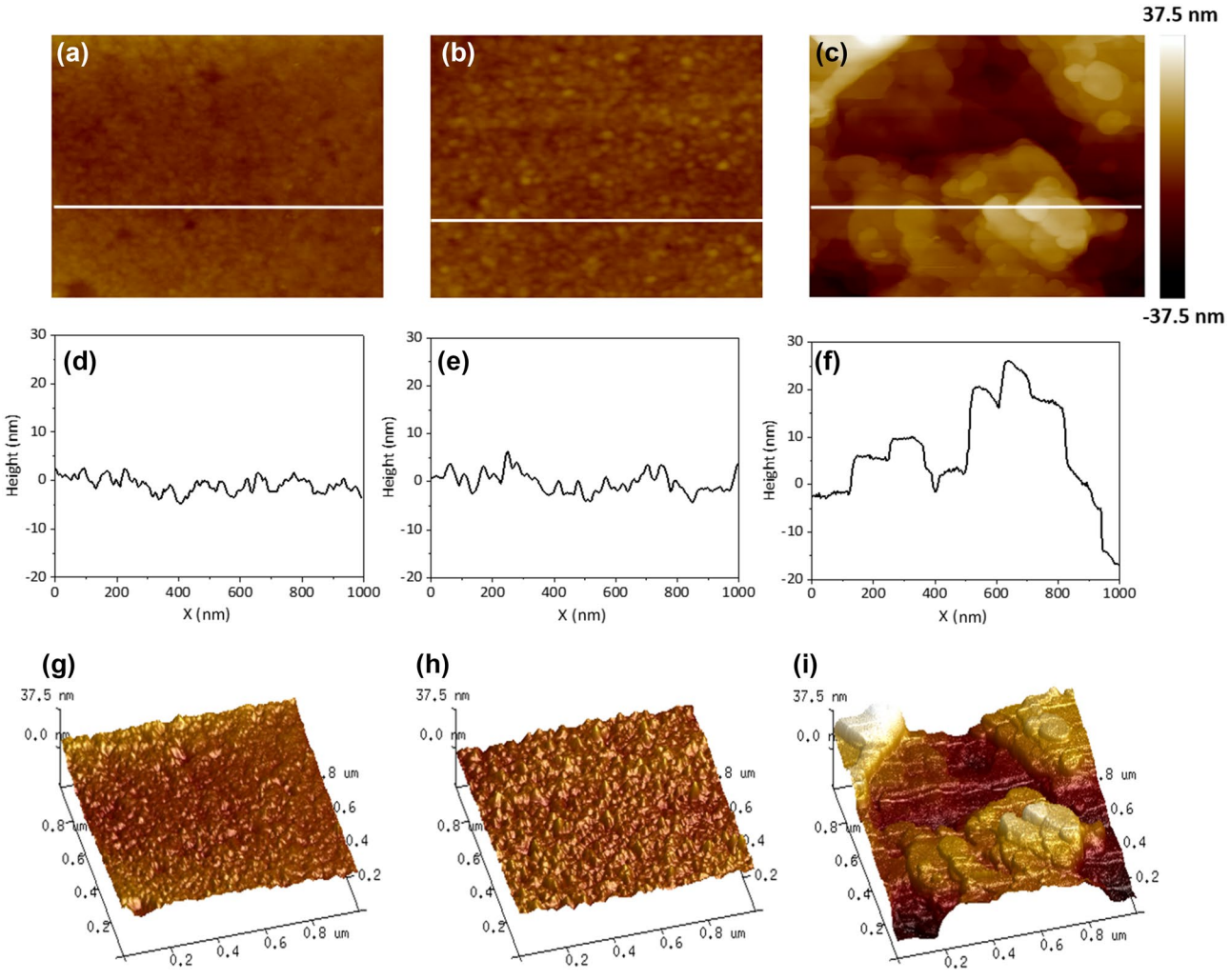

Fig. 3 **a–c** AFM phase images, **d–f** roughness profiles, and **g–i** 3D AFM micrographs of the surface morphology of PFSA, PFSA-NH-Zr-1, and PFSA-NH-Zr-10

first solid–solid transition stage (40 °C), indicating that there was an obvious entropy reduction behavior in the membrane, which was attributed to the transformation of molecular chain segments in the membrane from amorphous to ordered as the temperature rose to about 40 °C. Meanwhile, the results indicated there was a slight increase in the Tg of PFSA-NH-Zr-1 when the NH-Zr framework was incorporated into the PFSA matrix. This higher Tg was attributable to the -NH- groups and -SO_3H forming acid–base pairs via hydrogen bonding, which limited the movement of the PFSA side chains through their strong interactions and made the hybrid membrane better dimensional stable [61]. At the same time, Fig. 4d showed an increase in the binding energy of the pyrrolic N atom from 400.4 eV for PZDC to 402.6 eV for PFSA-NH-Zr-1, respectively. This transfer of energy indicated a change in electron distribution and the formation of acid–base interactions [62, 63].

3.3 Water uptake, swelling

Water uptake is a crucial property of PEMs as the water molecules are an essential proton carrier that could facilitate proton transport by engaging in the construction of hydrogen-bonding networks [64, 65]. We calculated the water uptake and swelling of all membranes according to Eqs. (1) and (2). With the increase of the NH-Zr framework, the water absorption of all membranes showed an increasing trend followed by a decreasing trend (Figs. 5a and S3). Compared to the pristine PFSA membrane (15.7%), the water absorption of the hybrid membrane increased from 17.7% for PFSA-NH-Zr-0.5 to 18,4% for PFSA-NH-Zr-1 and to the highest value of 21.2% for PFSA-NH-Zr-5. As the NH-Zr framework was rich in weakly acidic -NH- groups which could promote the collection of water, the introduction of the NH-Zr framework into the perfluorosulfonic acid matrix improved the membrane hydrophilicity. However, with the increase of NH-Zr framework loading content to 10 wt%, the water absorption of the hybrid membrane began to decrease, which might be due to the introduction of excessive NH-Zr framework leading to aggregation, thus limiting the introduction of water molecules and decreasing the water absorption of the hybrid membrane [66]. Nevertheless, the swelling of all hybrid membranes was reduced compared to the pristine PFSA membrane, mainly due to the rigid structure of the NH-Zr framework, which occupied a larger space within the membrane and restrained the movement of the polymer chains, resulting in less swelling of the membranes. Additionally, water contact angles were also measured to confirm the higher hydrophilicity of the PFSA-NH-Zr hybrid membranes (Figs. 5b and S3). The contact angle continued to decrease from 99.57° of the pristine PFSA membrane to 96.32° of the hybrid membrane (doping content is 5%) and then rose to 97.62° (doping content is 15%), where the contact angles of PFSA-NH-Zr-0.5, PFSA-NH-Zr-1, and

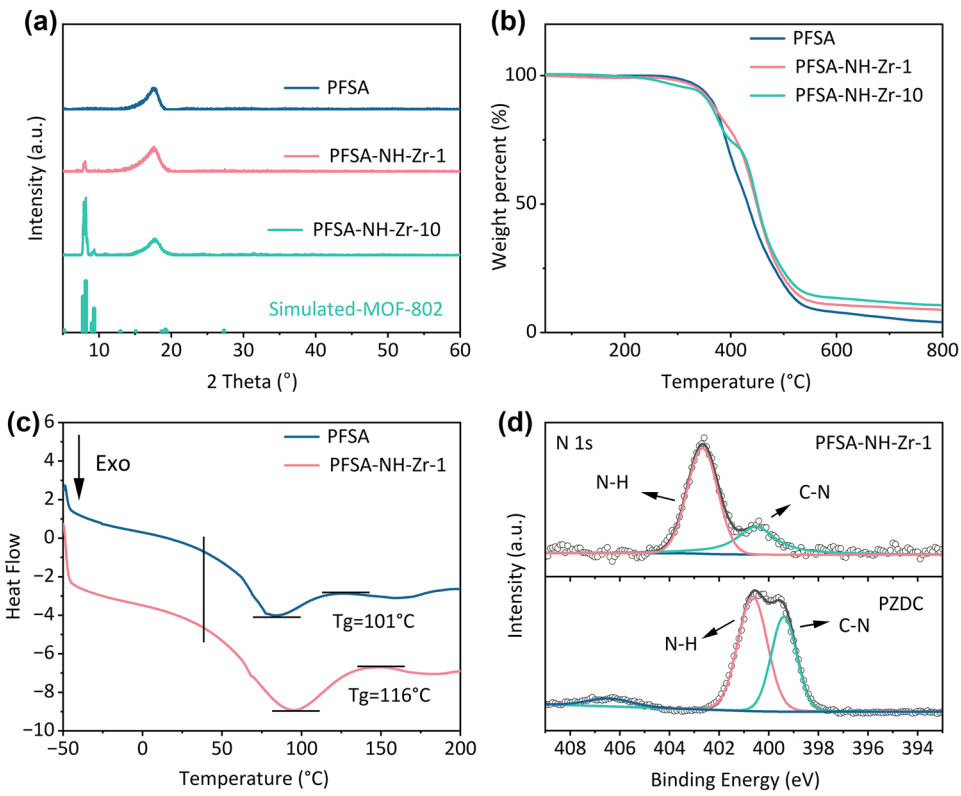

Fig. 4 Physiochemical properties of the pristine membrane and various hybrid membranes: **a** XRD patterns, **b** TGA curves, **c** DSC, and **d** high-resolution XPS of N 1 s peak

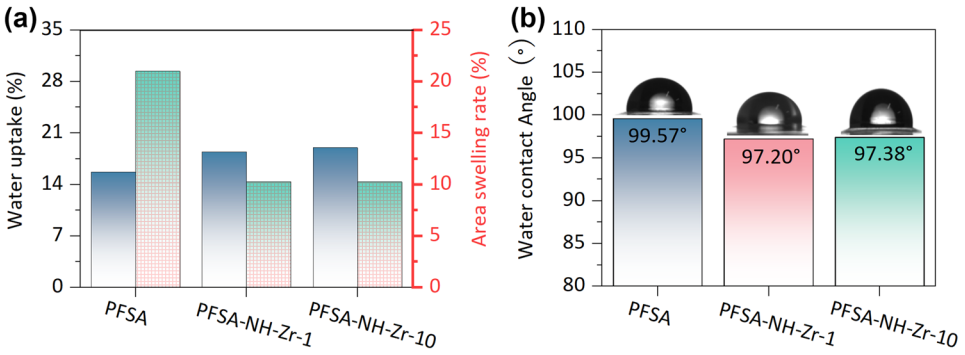

Fig. 5 **a** WUs, SRs, and **b** water contact angle of PFSA, PFSA-NH-Zr-1, and PFSA-NH-Zr-10

PFSA-NH-Zr-10 were 98.87°, 97.20°, and 97.38°. The contact angle of the PFSA-NH-Zr-5 hybrid membrane showed the smallest contact angle, indicating the increasing hydrophilicity due to the NH-Zr framework rich in weakly acidic -NH- groups that promoted the aggregation of water.

3.4 Proton conductivity test

The proton exchange membrane, the nucleus of the PEMFC, is responsible for transporting protons from the anode to the cathode, and the rate of proton transfer directly influences the overall performance of fuel cells. To compare the proton conductivity of the hybrid and pristine PFSA membranes, the proton conductivity of various membranes was measured according to Eq. (3) under temperature environments ranging from 30 to 90 °C at 100% RH. As an important note, the filler loading of the NH-Zr framework had a non-negligible impact on the proton conductivity of the hybrid membranes (Figs. 6a and S4). The conductivity increases to a maximum of 0.292 S/cm when the filler loading reached 1 wt%, which was 38% greater than the conductivity of the pristine PFSA membrane (0.209 S/cm) at 80 °C and 100% RH. This phenomenon could be explained by several factors: (i) Open metal sites (Zr^{4+}) in the NH-Zr framework could promote the protonation of water. (ii) -NH- in the NH-Zr framework could form enormous hydrogen-bonding networks with the sulfonic acid groups of PFSA, which renders the hydrophilic zones of PFSA more successive. By forming a long-range ordered hydration channel, proton migration turns easier and smoother, significantly improving the proton conductivity of the hybrid membranes. (iii) The combination of the sulfonic acid group with H_2O adsorbed at the NH-Zr framework interface may create an additional pathway for proton hopping motion. As the filler loading continued to rise from 5 to 15 wt%, the conductivity declined from 0.251 to 0.182 S/cm. This was probably due to the agglomeration of the low conductive filler (NH-Zr framework) and the partial covering of the sulfonic acid groups of the PFSA, followed by a decrease in the number of usable proton donors, which aggravated the connection of the proton transport pathways in the hybrid membranes.

The proton conductivity of all hybrid membranes declined slightly when the humidity was decreased to 40% (Figs. 6d and S6). This was mainly due to the decrease in water molecule adsorption caused by lower humidity, resulting in a reduction in proton conductivity. Even then, the conductivity of the PFSA-NH-Zr-1 membrane was still greater compared to that of the pristine PFSA membrane. The proton conductivity of the PFSA-NH-Zr-1 membrane was 0.031 S/cm under 40% RH and 80 °C, which was 34% greater compared to that of the pristine PFSA membrane (0.023 S/cm). This result was caused by the enhanced water absorption of the PFSA-NH-Zr hybrid membrane and the fast proton transport channel created by the acid–base pair.

Understanding the mechanism of proton transport in PEMs could help to design new PEMs materials. In general, the Grotthuss mechanism and the Vehicular mechanism are considered to be the two main mechanisms of proton conduction in PEMs. Typical activation energies for both Grotthuss and Vehicle proton transfer mechanisms have been reported to be between, respectively, 0.1–0.4 eV and 0.5–0.9 eV [67]. The activation energy (Ea) of proton conduction was calculated according to Eq. (4) for pristine PFSA membranes and various hybrid membranes based on the proton conductivity calculated from the heating cycle (Figs. 6b, S4b, and S5). It could be seen that the proton transport mechanism of the membrane changed significantly at about 40 °C. According to the DSC test result (Fig. 4c), the molecular arrangement in the membrane chain changed from disorder to order when the temperature rose to 40 °C, which made the proton transport channel in the membrane more regular and the proton transport more rapid and effective. We compared the activation energies of different membranes at 40 and 80 °C (Fig. 6b, c). The Ea values of pristine PFSA and hybrid membranes were between 0.68 and 0.9 eV in the temperature range of 30 to 40 °C, which indicated that the diffusion of protons in the membrane was more likely to the Vehicular mechanism. The Ea values of both PFSA-NH-Zr-1 and PFSA-NH-Zr-5 were lower than the pristine PFSA membrane due to the introduction of the NH-Zr framework increased the hydrophilicity of the membranes, resulting in

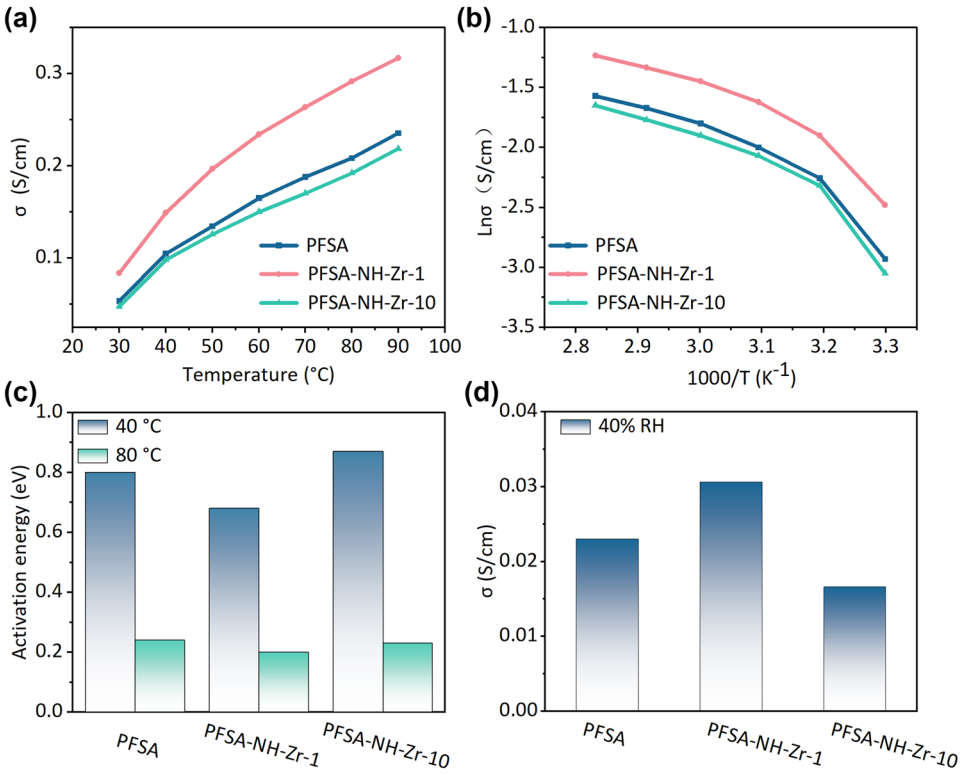

Fig. 6 Physicochemical properties of PFSA, PFSA-NH-Zr-1, and PFSA-NH-Zr-10. **a** Proton conductivity under 100% RH. **b** Activation energy. **c** Activation energy under 40 and 80 °C. **d** Proton conductivities under 80 °C and 40% RH

a lower energy barrier required for proton diffusion in the Vehicular mechanism. The Ea values of all the membranes were between 0.20 and 0.24 eV as the temperature rose to 50 °C, indicating a transition from the Vehicular mechanism to the Grotthuss mechanism. Therefore, the strong acid–base proton pair that started to form between the -NH- group of NH-Zr framework and the -SO_3H group of PFSA could construct low energy barrier channels in the process of proton transport and improve the efficiency of proton transport when the temperature reached about 40 °C. At the same time, the = N- groups contained in the NH-Zr framework could accept protons, adding additional proton transport sites, which ultimately led to the improvement of proton conductivity.

3.5 Single-cell test

Comprehensively, the fabricated MEAs with the PFSA-NH-Zr-0.5, PFSA-NH-Zr-1, PFSA-NH-Zr-5, and PFSA-NH-Zr-10 membranes were selected and their performances were evaluated in PEMFC, along with the pristine PFSA membrane for comparison. The measured power output and polarization curves were shown in Figs. 7a, c, and S7. In an H_2/Air single fuel cell, all the prepared PFSA-based membranes had high open-circuit voltages, indicating a lower fuel crossover and better electrode activity. The PFSA-NH-Zr-1 membrane showed significant improvement in cell performance at 80 °C and different humidification environments (40%, 100% RH). As shown in Fig. 7c, at 100% RH, the PFSA-NH-Zr-1 membrane achieved the maximum power density (P_{max}) of 784 mW/cm^2, which was 20% greater than the pristine PFSA membrane (656 mW/cm^2). At the same time, the P_{max} of all membranes gradually dropped with reducing RHs, which was mainly due to the decrease in conductivity resulting from the reduction in the number of water molecules as proton transport carriers, thus leading to the decline in cell performance. At 40% RH (Fig. 7a), the P_{max} of the PFSA-NH-Zr-1 membrane decreased to 0.726 W/cm^2, which was 20% higher compared to that of the pristine PFSA membrane (0.604 W/cm^2). This enhanced performance of the PFSA-NH-Zr-1 membrane was the result of a significant enhancement of proton conductivity in the hybrid membrane, which decreased the proton transfer resistance between electrodes. Meanwhile, Figs. 7b, d, and S7 showed that the internal resistance of all membranes remained stable during the single-cell performance test, indicating that all membranes remained stable during the test and that the PFSA-NH-Zr-1 membrane exhibited the lowest HFR value compared to the pristine PFSA and PFSA-NH-Zr-10 membranes, mainly due to the significantly higher proton conductivity.

EIS is a popular method for discerning the varying losses in fuel cell operation. The ohmic impedance of single cells assembled with pristine PFSA, PFSA-NH-Zr-1, and PFSA-NH-Zr-10 membranes was measured at 40% RH and 100% RH respectively. The arc intercept point on the Z′ axis at

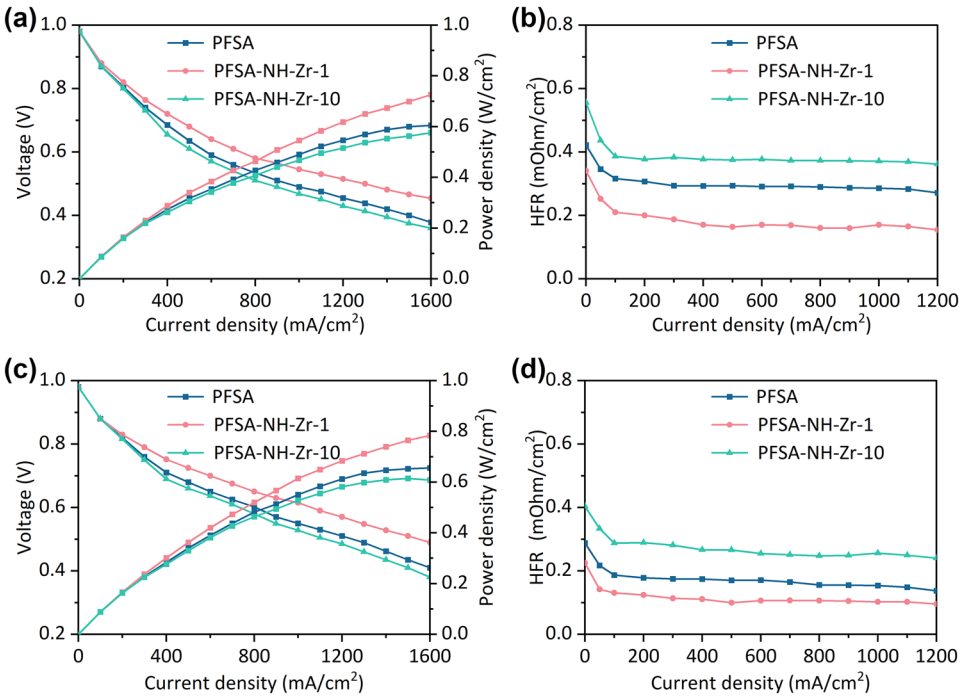

Fig. 7 Polarization curves of PEMFC of the tested membranes: at **a** 40% RH and **c** 100% RH. The current density of the membranes versus HFR at **b** 40% RH and **d** 100% RH

high frequency is considered to be the proton transport resistance in the membrane [68]. As could be shown from Fig. 8a, b, the pattern of ohmic resistance values of the three membranes was: PFSA-NH-Zr-1 < PFSA < PFSA-NH-Zr-10. We could find that PFSA-NH-Zr-1 had the lowest ohmic impedance at low RH due to its high proton conductivity. The -NH- in the NH-Zr framework could form a large hydrogen bonding network with the sulfonic acid groups of PFSA via acid–base pairs, allowing for faster and smoother proton migration, significantly improving proton conduction in the hybrid membranes and resulting in excellent cell performance. This demonstrated that the appropriate addition of NH-Zr framework to the proton exchange membrane could enhance the performance of the cell at low humidity

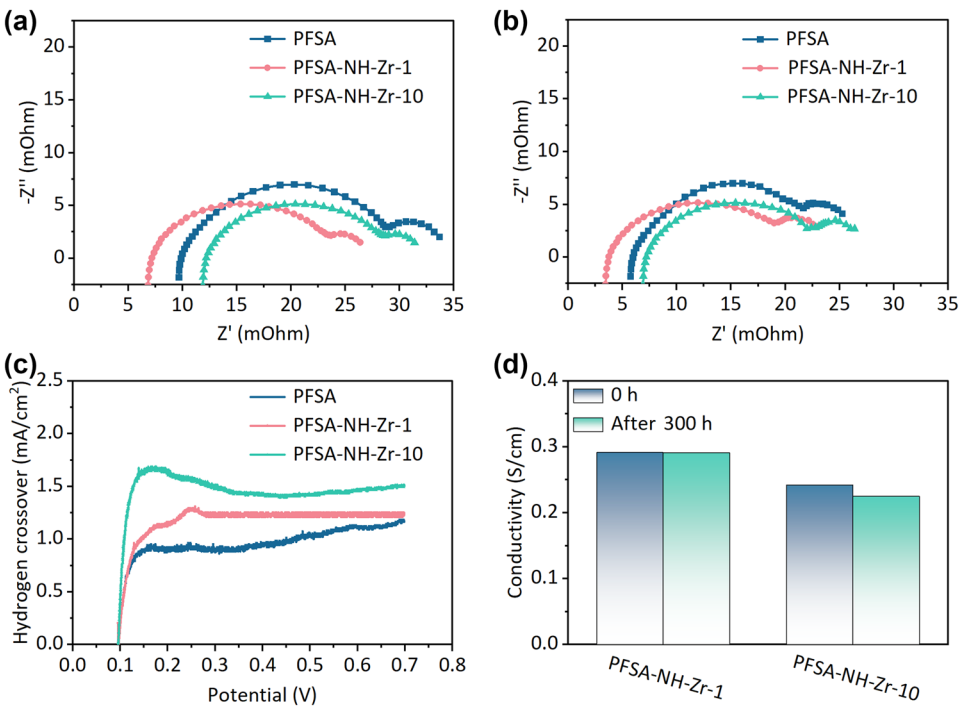

Fig. 8 Nyquist plots of membranes at **a** 40% RH and **b** 100% RH at 800 mA/cm^2. **c** Hydrogen crossover results of the membranes. **d** Time-dependent proton conductivity of membranes at 80 °C, 100% RH

Table 1 Comparative of proton conductivity and power density with other published PEMs [67, 73–80]

No.	Samples	T (°C)	RH (%)	Proton conductivity (S/cm)	Power density (W/cm^2)	Ref.
1	PFSA-NH-Zr-1	80	100	0.292	0.66	This work
2	p-BPAF@Nafion	80	100	0.256	0.11	[67]
3	PSS@ZIF-8–9	80	100	0.259	N/A	[73]
4	SP-ZIF-L@GO-5	70	100	0.265	0.65	[74]
5	Nafion-CeNT-0.5	80	100	0.123	0.90	[75]
6	ZIF-67@Nafion	80	100	0.288	0.30	[76]
7	Nafion/SNPAEK-7.5%	80	100	0.163	0.03	[77]
8	BUT-8(Cr)A	80	100	0.127	N/A	[78]
9	GO@UiO-66-NH_2/Nafion	90	95	0.303	N/A	[79]
10	P/ZIF-9@Nafion	75	100	0.258	0.15	[80]

conditions, depending on the introduction of water absorbing groups into the NH-Zr framework to achieve higher water retention at low humidity conditions, and acid–base proton pair interactions to achieve a more ordered proton transfer path [69].

The size and content of inorganic nanoparticles as well as the dispersion have an obvious influence on the gas permeability of the hybrid membrane [70–72]. Hydrogen crossover is the diffusion of hydrogen from the anode to the cathode, and the passing hydrogen could react directly with oxygen, resulting in lower battery voltage and possible production of hydrogen peroxide, which could result in chemical degradation. The density of hydrogen crossover-current could be used to characterize the degree of hydrogen penetration. Linear sweep voltammetry (LSV) was used to test the H_2 crossover-current density of pristine PFSA, PFSA-NH-Zr-1, and PFSA-NH-Zr-10 hybrid membranes, as presented in Fig. 8c. The data showed that the H_2 crossover-current density was higher with the addition of the porous NH-Zr framework to the hybrid membrane. In addition, the H_2 crossover-current density of the PFSA-NH-Zr-1 hybrid membrane (1.60 mA/cm^2) was lower than that of the PFSA-NH-Zr-10 hybrid membrane (1.88 mA/cm^2) under the same conditions. This was mainly attributed to the homogeneous and stable distribution of inorganic particles in PFSA-NH-Zr-1 in the hybrid membrane, achieving a more favorable organic–inorganic interface and thus inhibiting the penetration of hydrogen. Figure 8d showed the conductivity versus time for PFSA-NH-Zr-1 and PFSA-NH-Zr-10 at 80 °C and 100% RH. The results showed that the PFSA-NH-Zr-1 hybrid membrane maintained a high proton conductivity after 300 h, demonstrating positive conductivity stability, which might be attributed to the better dispersion and interfacial compatibility of the NH-Zr framework in the PFSA-NH-Zr-1 membrane, whereas the PFSA-NH-Zr-10 hybrid membrane exhibited a poor organic–inorganic interface due to particle agglomeration, and leaching of agglomerated particles occurred under prolonged water immersion, resulting in a decrease in proton conductivity.

Table 1 listed the conductivity and the maximum power density of PEMFCs for the hybrid membranes prepared in this work and the recently reported hybrid membranes. The conductivity and PEMFCs performance of the PFSA-N-Zr-1 hybrid membrane obtained in this study was compared with other PFSA-based (No. 2–No. 10) hybrid membranes that were modified with inorganic fillers. This result was effective in demonstrating that PEMFCs perform from PFSA-N-Zr-1 hybrid membranes better than reported organic–inorganic hybrid membranes recently.

4 Conclusions

In this study, PZDC and $ZrOCl_2{\cdot}8H_2O$ were incorporated into the PFSA solution and the NH-Zr framework structure rich in basic sites was constructed in situ, a series of hybrid membranes with variable contents of NH-Zr was successfully prepared, and the optimum contents were obtained. The introduced NH-Zr framework effectively induced the reorganization of the proton conducting group (-SO_3H) along the NH-Zr framework, thus constructing a fast ion transport channel. Meanwhile, the acid–base pairs between N–H (NH-Zr framework) and -SO_3H (PFSA) promoted the protonation/deprotonation and the subsequent proton leap through Grotthuss mechanisms under low humidity. We demonstrated that suitable content of NH-Zr was more likely to form harmonious acid–base pairs and continuous proton transport channels, which would maximize the facilitation of the NH-Zr framework in proton conduction. In particular, the PFSA-NH-Zr-1 hybrid membrane displayed superior proton conductivity, reaching 0.292 S/cm at 80 °C and 100% RH, and 0.031 S/cm under 80 °C, 40% RH. The maximum power density of the PFSA-NH-Zr-1 hybrid membrane reached 0. 726 W/cm^2 at low RH. The as-prepared PFSA-NH-Zr hybrid membranes also exhibited improvements in dimensional and thermal stability compared with the pristine PFSA membrane. It indicated that the PFSA-NH-Zr hybrid membrane has significant potential for high-performance PEM under low-humidity conditions.

Supplementary Information The online version contains supplementary material available at https://doi.org/10.1007/s42114-023-00637-0.

Author contribution Wenxing Zhang designed the study and collected the data. Shengqiu Zhao analysed most of the data and wrote the initial draft of the paper. Rui Wang, Aojie Zhang, and Yi Huang contributed to refining the ideas and carrying out additional analyses. Haolin Tang contributed the central idea and finalized this paper. Wenxing Zhang and Shengqiu Zhao contributed equally to this work. All authors reviewed the manuscript.

Funding This work was supported by the National Natural Science Foundation of China (T2241003).

Data availability Data available on request from the authors.

Declarations

Conflict of interest The authors declare no competing interests.

References

1. Bai H, Zhang J, Wang H, Xiang Y, Lu S (2022) Highly conductive quaternary ammonium-containing cross-linked poly (vinyl pyrrolidone) for high-temperature PEM fuel cells with high-performance. J Membr Sci 645:120194
2. Chen L, Nie Y, Yu H, Tao W (2020) Study on the mechanism of destruction triggering of membrane electrode assembly of hydrogen fuel cell. Int J Heat Mass Transfer 159:120144
3. Jin F, Yan K, Zhao Y, Du L, Li R, Zheng J, Wang T, Feng Z (2020) Surface enriched sulfonic acid ionic clusters of nafion nanofibers as long-range interconnected ionic nanochannels for anisotropic proton transportation: phenomenon and molecular mechanism. Adv Mater Interfaces 7:2000342
4. Zhao S, Wang R, Tian T, Liu H, Zhang H, Tang H (2022) Self-assembly-cooperating in situ construction of MXene-CeO_2 as hybrid membrane coating for durable and high-performance proton exchange membrane fuel cell. ACS Sustainable Chem Eng 10:4269–4278
5. Wang B, Sun X, Xie X, Wang J, Li L, Jiao K (2021) Experimental investigation of a novel cathode matrix flow field in proton exchange membrane fuel cell. ES Energy Environ 12:95–107
6. Liu H, Guo L, Liu M, Chen H, Han W, Bian H, Tian X, Wang C, Guo Z, Sun J (2022) Water management simulation of proton exchange membrane fuel cells with micro-ribs based on volume of fluid model. ES Energy Environ 15:45–55
7. Tian T, Cheng Y, Sun Z, Huang K, Lei M, Tang H (2023) Carbon nanotubes supported oxygen reduction reaction catalysts: role of inner tubes. Adv Compos Hybrid Mater 6:7
8. Hou C, Wang B, Murugadoss V, Vupputuri S, Chao Y, Guo Z, Wang C, Du W (2020) Recent advances in Co_3O_4 as anode materials for high-performance lithium-ion batteries. Eng Sci 11:19–30
9. Yang W, Peng D, Kimura H, Zhang X, Sun X, Pashmeah R, Alzahrani E, Wang B, Guo Z, Du W, Hou C (2022) Honeycomb-like nitrogen-doped porous carbon decorated with Co_3O_4 nanoparticles for superior electrochemical performance pseudocapacitive lithium storage and supercapacitors. Adv Compos Hybrid Mate 5:3146–3157
10. Qiu W, Hao Q, Annamareddy S, Xu B, Guo Z, Jiang Q (2022) Electric vehicle revolution and implications: ion battery and energy. Eng Sci 20:100–109
11. Lian M, Sun J, Jiang D, Xu M, Wu Z, Xu B, Algadi H, Huang M, Guo Z (2022) Waterwheel-inspired high-performance hybrid electromagnetic-triboelectric nanogenerators based on fluid pipeline energy harvesting for power supply systems and data monitoring. Nanotechnol 34:2
12. Gao S, Zhao X, Fu Q, Zhang T, Zhu J, Hou F, Ni J, Zhu C, Li T, Wang Y, Murugadoss V, Mersal G, Ibrahim M, EI-Bahy Z, Huang M, Guo Z (2022) Highly transmitted silver nanowires-SWCNTs conductive flexible film by nested density structure and aluminum-doped zinc oxide capping layer for flexible amorphous silicon solar cells. J Mater Sci Technol 126:152–160
13. Wang R, Meng Z, Yan X, Tian T, Lei M, Pashameah R, Abo-Dief H, Algadi H, Huang N, Guo Z, Tang H (2023) Tellurium intervened Fe-N codoped carbon for improved oxygen reduction reaction and high-performance Zn-air batteries. J Mater Sci Technol 137:215–222
14. Han J, Kim K, Kim S, Lee H, Kim J, Ko T, Bae J, Choi W, Sung Y, Lee J (2020) Cross-linked sulfonated poly(ether ether ketone) membranes formed by poly(2,5-benzimidazole)-grafted graphene oxide as a novel cross-linker for direct methanol fuel cell applications. J Power Sources 448:227427
15. Huang X, Zhao S, Liu H, Wang R, Tang H (2022) Hydrophilic channel volume behavior on proton transport performance of proton exchange membrane in fuel cells. ACS Appl Polym Mater 4:2423–2431
16. Kim A, Vinothkannan M, Song M, Lee J, Lee H, Yoo D (2020) Amine functionalized carbon nanotube (ACNT) filled in sulfonated poly (ether ether ketone) membrane: Effects of ACNT in improving polymer electrolyte fuel cell performance under reduced relative humidity. Compos B 188:107890
17. Wang L, Deng N, Wang G, Ju J, Cheng B, Kang W (2019) Constructing amino-functionalized flower-like metal organic framework nanofibers in sulfonated poly(ether sulfone) proton exchange membrane for simultaneously enhancing interface compatibility and proton conduction. ACS Appl Mater Interfaces 11:39979–39990
18. Zhao G, Xu X, Shi L, Cheng B, Zhuang X, Yin Y (2020) Biofunctionalized nanofiber hybrid proton exchange membrane based on acid-base ion-nanochannels with superior proton conductivity. J Power Sources 452:227839
19. Li G, Shen R, Hu S, Wang B, Algadi H, Wang C (2022) Norbornene-based acid-base blended polymer membranes with low ion exchange capacity for proton exchange membrane fuel cell. Adv Compos Hybrid Mater 5:2131–2137
20. Yang J, Tong L, Alsubaie A, Mahmoud K, Guo Y, Liu L, Guo L, Sun Z, Wang C (2022) Hybrid proton exchange membrane used in fuel cell with amino-functionalized metal-organic framework in sulfonated polyimide to construct efficient ion transport channel. Adv Compos Hybrid Mater 5:834–842
21. Hamid N, Kamarudin S, Karim N (2021) Potential of Nafion/eggshell composite membrane for application in direct methanol fuel cell. Int J Energy Res 45:2245–2264
22. Passalacqua E, Pedicini R, Carbone A, Gatto I, Matera F, Patti A, Sacca A (2020) Effects of the chemical treatment on the physical-chemical and electrochemical properties of the commercial nafion (TM) NR212 Membrane. Mater 13:5254
23. Yin C, He C, Liu Q, Xiong B, Li J, Zhou Y (2021) Effect of the orientation of sulfonated graphene oxide (SG) on the gas-barrier properties and proton conductivity of a SG/Nafion composite membrane. J Membr Sci 625:119146
24. Zizhou R, Cay A, Kumbasar E, Colpan C (2021) Production of poly(vinyl alcohol)/Nafion (R) nanofibers and their stability assessment for the use in direct methanol fuel cells. J Ind Text 50:773–793
25. Guo Y, Jiang Z, Ying W, Chen L, Liu Y, Wang X, Jiang Z, Chen B, Peng X (2018) A DNA-threaded ZIF-8 membrane with high proton conductivity and low methanol permeability. Adv Mater 30:1705155

26. Giffin G, Haugen G, Hamrock S, Di Noto V (2013) Interplay between structure and relaxations in perfluorosulfonic acid proton conducting membranes. J Am Chem Soc 135:822–834
27. Hou J, Li J, Mountz D, Hull M, Madsen L (2013) Correlating morphology, proton conductivity, and water transport in polyelectrolyte-fluoropolymer blend membranes. J Membr Sci 448:292–299
28. Kreuer K, Portale G (2013) A critical revision of the nano-morphology of proton conducting ionomers and polyelectrolytes for fuel cell applications. Adv Funct Mater 23:5390–5397
29. Li N, Guiver M (2014) Ion transport by nanochannels in ion-containing aromatic copolymers. Macromol 47:2175–2198
30. Park C, Lee S, Hwang D, Shin D, Cho D, Lee K, Kim T, Kim T, Lee M, Kim D, Doherty C, Thornton A, Hill A, Guiver M, Lee Y (2016) Nanocrack-regulated self-humidifying membranes. Nat 532:480–483
31. Tohidian M, Ghaffarian S (2017) Polyelectrolyte nanocomposite membranes with imidazole-functionalized multi-walled carbon nanotubes for use in fuel cell applications. J Macromol Sci Part B: Phys 56:725–738
32. Huang Z, Lv B, Zhou L, Wei T, Qin X, Shao Z (2022) Ultra-thin h-BN doped high sulfonation sulfonated poly (ether-ether-ketone) of PTFE-reinforced proton exchange membrane. J Membr Sci 644:120099
33. Park S, Lee D, Kang Y (2010) High temperature proton exchange membranes based on triazoles attached onto SBA-15 type mesoporous silica. J Membr Sci 357:1–5
34. He X, He G, Zhao A, Wang F, Mao X, Yin Y, Cao L, Zhang B, Wu H, Jiang Z (2017) Facilitating proton transport in nafion-based membranes at low humidity by incorporating multifunctional graphene oxide nanosheets. ACS Appl Mater Interfaces 9:27676–27687
35. Ye G, Hayden C, Goward G (2007) Proton dynamics of nafion and Nafion/SiO_2 composites by solid state NMR and pulse field gradient NMR. Macromol 40:1529–1537
36. Kuang T, Zhang M, Chen F, Fei Y, Yang J, Zhong M, Wu B, Liu T (2023) Creating poly(lactic acid)/carbon nanotubes/carbon black nanocomposites with high electrical conductivity and good mechanical properties by constructing a segregated double network with a low content of hybrid nanofiller. Adv Compos Hybrid Mater 6:48
37. Zhang Z, Liu M, Ibrahim M, Wu H, Wu Y, Li Y, Mersal G, El-Azab I, El-Bahy S, Huang M, Jiang Y, Liang G, Xie P, Liu C (2022) Flexible polystyrene/graphene composites with epsilon-near-zero properties. Adv Compos Hybrid Mater 5:1054–1066
38. Xie P, Shi Z, Feng M, Sun K, Liu Y, Yan K, Liu C, Moussa T, Huang M, Meng S, Liang G, Hou H, Fan R, Guo Z (2022) Recent Advances in radio-frequency negative dielectric metamaterials by designing heterogeneous composites. Adv Compos Hybrid Mater 5:679–695
39. Liu M, Wu H, Wu Y, Xie P, Pashameah R, Abo-Dief H, El-Bahy S, Wei Y, Li G, Li W, Liang G, Liu C, Sun K, Fan R (2022) The weakly negative permittivity with low-frequency-dispersion behavior in percolative carbon nanotubes/epoxy nanocomposites at radio-frequency range. Adv Compos Hybrid Mater 5:2021–2030
40. Xie P, Liu Y, Feng M, Niu M, Liu C, Wu N, Sui K, Patil R, Pan D, Guo Z, Fan R (2021) Hierarchically porous Co/C nanocomposites for ultralight high-performance microwave absorption. Adv Compos Hybrid Mater 4:173–185
41. Lu J, Tang H, Lu S, Wu H, Jiang S (2011) A novel inorganic proton exchange membrane based on self-assembled HPW-meso-silica for direct methanol fuel cells. J Mater Chem 21:6668–6676
42. Tang H, Wan Z, Pan M, Jiang S (2007) Self-assembled Nafion-silica nanoparticles for elevated-high temperature polymer electrolyte membrane fuel cells. Electrochem Commun 9:2003–2008
43. Patel H, Mansor N, Gadipelli S, Brett D, Guo Z (2016) Superacidity in Nafion/MOF hybrid membranes retains water at low humidity to enhance proton conduction for fuel cells. ACS Appl Mater Interfaces 8:30687–30691
44. Li J, Xu G, Cai W, Xiong J, Ma L, Yang Z, Huang Y, Cheng H (2018) Non-destructive modification on Nafion membrane via in-situ inserting of sheared graphene oxide for direct methanol fuel cell applications. Electrochim Acta 282:362–368
45. Li J, Xu G, Luo X, Xiong J, Liu Z, Cai W (2018) Effect of nano-size of functionalized silica on overall performance of swelling-filling modified Nafion membrane for direct methanol fuel cell application. Appl Energy 213:408–414
46. Li Z, Huang H, Zhu J, Wu J, Yang H, Wei L, Guo X (2019) Ionic conduction in composite polymer electrolytes: case of PEO: Ga-LLZO composites. ACS Appl Mater Interfaces 11:784–791
47. Zhou Q, Ma J, Dong S, Li X, Cui G (2019) Intermolecular chemistry in solid polymer electrolytes for high-energy-density lithium batteries. Adv Mater 31:1902029
48. Liu W, Luo N, Li P, Yang X, Dai Z, Song S, Wei J, Zhang H (2020) New sulfonated poly (ether ether ketone) composite membrane with the spherical bell-typed superabsorbent microspheres: excellent proton conductivity and water retention properties at low humidity. J Power Sources 452:227823
49. Rao Z, Lan M, Wang Z, Wan H, Li G, Zhu J, Tang B, Liu H (2022) Effectively facilitating the proton conduction of proton exchange membrane by polydopamine modified hollow metal-organic framework. J Membr Sci 644:120098
50. Khatua S, Bar A, Sheikh J, Clearfield A, Konar S (2018) Achieving amphibious superprotonic conductivity in a Cu-I metal-organic framework by strategic pyrazinium salt impregnation. Chem - Eur J 24:872–880
51. Phang W, Jo H, Lee W, Song J, Yoo K, Kim B, Hong C (2015) Superprotonic conductivity of a UiO-66 Framework functionalized with sulfonic acid groups by facile postsynthetic oxidation. Angew Chem Int Ed 54:5142–5146
52. Yang F, Huang H, Wang X, Li F, Gong Y, Zhong C, Li J (2015) Proton conductivities in functionalized UiO-66: tuned properties, thermogravimetry mass, and molecular simulation analyses. Cryst Growth Des 15:5827–5833
53. Yoshida Y, Kitagawa H (2019) Ionic conduction in metal-organic frameworks with incorporated ionic liquids. ACS Sustainable Chem Eng 7:70–81
54. Zhang F, Dong L, Qin J, Guan W, Liu J, Li S, Lu M, Lan Y, Su Z, Zhou H (2017) Effect of Imidazole arrangements on proton-conductivity in metal-organic frameworks. J Am Chem Soc 139:6183–6189
55. Xue R, Guo H, Yang W, Huang S, Yang G (2022) Cooperation between covalent organic frameworks (COFs) and metal organic frameworks (MOFs): application of COFs-MOFs hybrids. Adv Compos Hybrid Mater 5:1595–1611
56. Feng S, Zhai F, Su H, Sridhar D, Algadi H, Xu B, Pashameah R, Alzahrani E, Abo-Dief H, Ma Y, Li T, Guo Z (2023) Progress of metal organic frameworks-based composites in electromagnetic wave absorption. Mater Today Phys 30:100950
57. Jing C, Zhang Y, Zheng J, Ge S, Lin J, Pan D, Naik N, Guo Z (2022) In-situ constructing visible light CdS/Cd-MOF photocatalyst with enhanced photodegradation of methylene blue. Particuology 69:111–222
58. Yang X, Fan W, Wang H, Shi Y, Wang S, Liew R, Ge S (2022) Recycling of bast textile wastes into high value-added products: a review. Environ Chem Lett 20:3747–3763
59. Ge S, Zuo S, Zhang M, Luo Y, Yang R, Wu Y, Zhang Y, Li J, Xia C (2021) Utilization of decayed wood for polyvinyl chloride/wood flour composites. J Mater Res Technol 12:862–869
60. Ge S, Ma N, Jiang S, Ok Y, Lam S, Li C, Shi S, Nie X, Qiu Y, Li D, Wu Q, Tsang D, Peng W, Sonne C (2020) Processed bamboo

as a novel formaldehyde-free high-performance furniture biocomposite. ACS Appl Mater Interfaces 12:30824–30832
61. Li Z, He G, Zhang B, Cao Y, Wu H, Jiang Z, Zhou T (2014) Enhanced proton conductivity of Nafion hybrid membrane under different humidities by incorporating metal-organic frameworks with high phytic acid loading. ACS Appl Mater Interfaces 6:9799–9807
62. Duan Y, Ru C, Li J, Sun Y, Pu X, Liu B, Pang B, Zhao C (2022) Enhancing proton conductivity and methanol resistance of SPAEK membrane by incorporating MOF with flexible alkyl sulfonic acid for DMFC. J Membr Sci 641:119906
63. Wang J, Liu Y, Dang J, Zhou G, Wang Y, Zhang Y, Qu L, Wu W (2020) Lamellar composite membrane with acid-base pair anchored layer-by-layer structure towards highly enhanced conductivity and stability. J Membr Sci 602:117978
64. Peckham T, Holdcroft S (2010) Structure-morphology-property relationships of non-perfluorinated proton-conducting membranes. Adv Mater 22:4667–4690
65. Xu J, Zhang Z, Yang K, He W, Yang X, Du X, Meng L, Zhao P, Wang Z (2020) Construction of new transport channels by blending POM-based inorganic-organic complex into sulfonated poly(ether ketone sulfone) for proton exchange membrane fuel cells. J Membr Sci 596:117711
66. Ru C, Li Z, Zhao C, Duan Y, Zhuang Z, Bu F, Na H (2018) Enhanced Proton Conductivity of Sulfonated Hybrid Poly(arylene ether ketone) Membranes by incorporating an amino-sulfo bifunctionalized metal-organic framework for direct methanol fuel cells. ACS Appl Mater Interfaces 10:7963–7973
67. Ru C, Gu Y, Duan Y, Zhao C, Na H (2019) Enhancement in proton conductivity and methanol resistance of Nafion membrane induced by blending sulfonated poly(arylene ether ketones) for direct methanol fuel cells. J Membr Sci 573:439–447
68. Wang H, Zhao Y, Shao Z, Xu W, Wu Q, Ding X, Hou H (2021) Proton conduction of Nafion hybrid membranes promoted by NH_3-Modified Zn-MOF with host-guest collaborative hydrogen bonds for H_2/O_2 fuel cell applications. ACS Appl Mater Interfaces 13:7485–7497
69. Lee K, Chu J, Kim A, Yoo D (2019) Effect of functionalized SiO_2 toward proton conductivity of composite membranes for PEMFC application. Int J Energy Res 43:5333–5345
70. Ghadimi A, Norouzbahari S, Sadrzadeh M, Mohammadi T (2012) Improvement in gas separation properties of a polymeric membrane through the incorporation of inorganic nano-particles. Polym Adv Technol 23:1101–1111
71. Hou C, Yang W, Kimura H, Xie X, Zhang X, Sun X, Yu Z, Yang X, Zhang Y, Wang B, Xu B, Sridhar D, Algadi H, Guo Z, Du W (2023) Boosted lithium storage performance by local build-in electric field derived by oxygen vacancies in 3D holey N-doped carbon structure decorated with molybdenum dioxide. J Mater Sci Technol 142:185–195
72. Li F, Li Q, Kimura H, Xie X, Zhang X, Wu N, Sun X, Xu B, Algadi H, Pashameah R, Alanazi A, Alzahrani E, Li H, Du W, Guo Z, Hou C (2022) Morphology controllable urchin-shaped bimetallic nickel-cobalt oxide/carbon composites with enhanced electromagnetic wave absorption performance. J Mater Sci Technol
73. Cai Y, Yang Q, Zhu Z, Sun Q, Zhu A, Zhang Q, Liu Q (2019) Achieving efficient proton conduction in a MOF-based proton exchange membrane through an encapsulation strategy. J Membr Sci 590:117277
74. Cai Y, Zhang Q, Zhu A, Liu Q (2021) Two-dimensional metal-organic framework-graphene oxide hybrid nanocomposite proton exchange membranes with enhanced proton conduction. J Colloid Interface Sci 594:593–603
75. Ketpang K, Oh K, Lim S, Shanmugam S (2016) Nafion-porous cerium oxide nanotubes composite membrane for polymer electrolyte fuel cells operated under dry conditions. J Power Sources 329:441–449
76. Rao Z, Feng K, Tang B, Wu P (2017) Construction of well interconnected metal-organic framework structure for effectively promoting proton conductivity of proton exchange membrane. J Membr Sci 533:160–170
77. Wang B, Hong L, Li Y, Zhao L, Zhao C, Na H (2017) Property enhancement effects of side-chain-type naphthalene based sulfonated poly(arylene ether ketone) on Nafion composite membranes for direct methanol fuel cells. ACS Appl Mater Interfaces 9:32227–32236
78. Yang F, Xu G, Dou Y, Wang B, Zhang H, Wu H, Zhou W, Li J, Chen B (2017) A flexible metal-organic framework with a high density of sulfonic acid sites for proton conduction. Nat Energy 2
79. Zhao G, Shi L, Zhang M, Cheng B, Yang G, Zhuang X (2021) Self-assembly of metal-organic framework onto nanofibrous mats to enhance proton conductivity for proton exchange membrane. Int J Hydrogen Energy 46:36415–36423
80. Zhao G, Xu X, Zhao H, Shi L, Zhuang X, Cheng B, Yin Y (2020) Zeolitic imidazolate framework decorated on 3D nanofiber network towards superior proton conduction for proton exchange membrane. J Membr Sci 601:117914